A strong lateral shear velocity gradient and anisotropy heterogeneity in the lowermost mantle beneath the southern Pacific

Sean R. Ford

Department of Geological Sciences, Arizona State University, Tempe, Arizona, USA

Now at Department of Earth and Planetary Science, University of California, Berkeley, California, USA

Edward J. Garnero and Allen K. McNamara

Arizona State University, Department of Geological Sciences, Tempe, Arizona, USA

Introduction

Figure S1 illustrates the difficulties in selecting high quality data, where care must be taken to avoid interference with depth and converted phases.

Figure S2 shows the geographic distribution of dT(SKKS-SKS) at CMB entry and exit points, and a general agreement with the trend in the tomography model SAW24B16, though the amplitude of the anomaly is not well matched. It is difficult to quantify the relative contribution to dT(SKKS-SKS) from either the eastern of western borders due to the ambiguity imparted by our limited azimuthal sampling. Two plausible scenarios exist. SKS could arrive earlier due to higher velocities (than tomographically predicted) in the eastern portion of our study area, while SKKS is delayed more than SKS in the western portion of our study area. In this case, the transition from low velocity to average (or high) velocities in the deepest mantle would have to occur over a much smaller scale than depicted in tomography at present, and quite low velocities must persist to the southwest of the lowest velocities in the tomographic predictions, toward the transition to average wavespeeds.

In this study, we employed several tests to assess the ability of our data to detect edges to the low velocity material north of 50degS in our study region (Figures S3a-S3e). Motivated by several studies of the south African anomaly [Ritsema et al., 1999; Wen, 2001; Ni and Helmberger, 2003], we experimented with enhancing the D" shear velocity reduction in an existing tomographic model at various cut-off levels to assess the effect of imposed sharp decreases in shear velocity over a short lateral scale length. If the enhanced tomographic model predicts dVs for the raypaths of our data that are similar to

our observations, we can then infer a possible location, shape, and magnitude to the low velocity material in the southern Pacific. Here, we solely employed SAW24B16, and note that to the first-order, the shear models introduced here are similar; we thus expect similar results for the other tomographic models. First, all velocities less than -1% perturbation from PREM were decreased by 3% (Figure S3c) and dT(S-SKS) was found by ray-tracing the same raypaths as our data through the new D" model. These dT(S-SKS) were then path-averaged as described above to find dVs. This same process was repeated with a decrease of 3% at velocity perturbations of -0.5% (Figure S3d), and at 0% (Figure S3e). Changing the dVs at which we impose a negative 3% step has the effect of moving the boundary of the very low velocity structure toward the center of our path coverage where the south-to-north latitudinal dependence of the velocity contrast can be exploited by our analysis. As the boundary is moved, dVs at raypath midpoint latitudes north of 45degS increases substantially. This large negative slope is not replicated in our observations and we conclude that if there is a low velocity structure with steep boundaries, it does not have the geometry of any of the models in Figure S3. In comparison with the dVs predicted by the enhanced tomographic models in Figures S3c-S3e, our observed dVs begins its decrease at raypath midpoint latitudes north of 50degS and has a much more constant slope; similar to that produced by SAW24B16 (Figure S3b), but with greater magnitude. Therefore, though the observed dependence of dVs on raypath midpoint latitude does not necessarily infer a low-velocity structure with vertical boundaries, it certainly suggests a rapid decrease in the velocity near the margins of this structure at the base of the mantle north of 50degS latitude. The predominately east-to-west raypath coverage of the southern Pacific and path average dVs approximation does not allow for any more of a constraint on the location of the anomalous structure.

To further explore the spatial velocity trends, we calculate a moving cap-average of dVs throughout the study area as in Wysession [1996]. The cap-averaged results accentuate a velocity increase from northwest to southeast, but serve to mute the complexity in the center of the study area. See Figure S4. Cap-averaging the velocity heterogeneity agrees best with model TXBW.

To better understand anisotropy throughout all of D" in our region we cap-average the data after distributing ks along whole D" raypaths (Figure S4b). The cap-averaging essentially applies a spatial low-pass filter to our data, and some smearing of ks due to the limited azimuthal sampling of our region is apparent. Comparison of the cap-averaged results with SAW24AN16 shows poor correlation in the center of the study area, but the positive cap-averaged ks in the northern region are somewhat corroborated by the tomography.

We compared data where both dT(S-SKS) and T(SV-SH) are measured and found no clear correlation between estimates of heterogeneity and anisotropy (Figures S4c-S4d). We also compared dVs and ks for every 4deg of our cap-averaged results, and again, find no clear positive correlation To further investigate a possible correlation we compare the dVs from SAW24B16 and the ks from SAW24AN16 at both the raypath midpoint location of our data, and at every 4deg (Figures S4c-S4d). Both renderings lack any clear positive correlation.

1. 2004JB003574-fsa01.eps (Figure S1) Examples of SV (solid lines) and SH (dashed lines) component waveforms that produce lower quality differential travel-time measurements. Traces are normalized in time to the SKS arrival, and scaled to the maximum amplitude of each trace. Important phases are noted and station, distance, and event (EV# corresponding to the first column in Table 1 in the printed text) information is listed to the right of the traces. (a) Signal to noise ratio is too low. This is especially the case with the SH component where no reliable SSH arrival time measurement can be made. (b) The onset of S or SKS is too emergent, in this case on the SV component. (c) The source is complex. (d) sSKS arrives coincident with S(SV). (e) At large distances, S(SV) is either weak or not present. (f) There is cross-component SKS contamination even after correcting for upper mantle anisotropy.

2. 2004JB003574-fa02.eps (Figure S2) PREM-calculated CMB piercing points of SKS (small, blue crosses) and SKKS (red circles and blue crosses, scaled in size according to SKKS-SKS travel time residuals). Residuals are observed minus PREM, and positive values indicate a relatively delayed SKKS or advanced SKS, and just the opposite for negative residuals. Short green line segments connect the SKS and SKKS CMB piercing points. D" velocity heterogeneity of SAW24B16 [Megnin and Romanowicz, 2000] is also shown, with dVs contour lines at +/-1 % intervals; dVs < -1% is shaded light grey, and dVs > 1% is shaded dark grey.

3. 2004JB003574-fs03.eps (Figure S3) (a) Map of great-circle raypaths of the data with projection and symbols as in Figure 1b in the printed text. Middle panel is of S-SKS travel-time residuals (dT(S-SKS)) as a function of raypath midpoint latitude. Open red circles are raw dT(S-SKS) with respect to PREM and solid black squares are dT(S-SKS) corrected with the velocity structure of model SAW24B16 [Megnin and Romanowicz, 2000]. SKS is corrected for the whole mantle structure and S is corrected for mantle structure above 2591 km (300 km thick D"). Bottom panel is estimated dVs as a function of raypath midpoint latitude. dVs inferred from uncorrected dT(S-SKS) (open red circles) and corrected dT(S-SKS) (black squares) found in the middle panels. 5deg bin averages of the uncorrected and corrected dVs (large light yellow circles and dark grey squares, respectively) with +/-1 standard deviation are also shown. (b-e) Top panels are D" velocity models where grey shading is dVs < -3% and negative 1% (red lines), and positive 1% (blue lines) dVs contour lines are shown. The solid black line represents 0% PREM velocity perturbation. Middle panels plot the dT(S-SKS) obtained by tracing the raypaths of the data through the velocity models shown in the top panels. dT(S-SKS) is either uncorrected (open red circles) or corrected (black squares) as previously described. Bottom panels are the inferred dVs obtained from the uncorrected or corrected dT(S-SKS) (large yellow circles and dark grey squares, respectively) and shown in the middle panels. 5deg bin averages of the uncorrected and corrected dVs (large yellow circles and dark grey squares, respectively) with +/-1 standard deviation are also shown. The D" shear velocity models are: (b) SAW24B16; (c) Modified SAW24B16 where all dVs < -1% are decreased by 3%; (d) Modified SAW24B16 where all dVs < 0.5% are decreased by 3%; and (e) Modified SAW24B16 where all negative dVs is decreased by 3%. The data shown in (a) predict a stronger lateral velocity gradient than shown in (b) or (c)

beginning near 50degS. However, the steep negative slopes of dVs versus raypath midpoint latitude in (d) and (e) are not replicated in (a).

4. 2004JB003574-fs04.eps (Figure S4) (a) Cap-averaged velocity heterogeneity dVs for region outlined in the inset globe in Figure 5a in printed text. A Gaussian cap radius of 5deg (~300 km at the CMB) was used in the averaging. Circles and crosses are lower and higher than average velocities, respectively. These are plotted on the D" velocity model, TXBW [Grand, 2002]. (b) Cap-averaged anisotropy ks for the same region as in (a), with the same cap radius. Circles and crosses represent V(SV) > V(SH) and V(SV) < V(SH), respectively. These values are plotted on top of the D" anisotropy model, SAW24AN16 [Panning and Romanowicz, 2005, in review]. (c) dVs versus ks for our data (crosses) where both measurements can be made, and also for tomographically derived dVs from SAW24B16 and ks from SAW24AN16 (circles), at the raypath midpoints of our data. (d) Cap-averaged values of dVs versus ks for our data (crosses) at 4deg intervals, and for the same models in (c) at the same 4deg interval locations (circles).

References

Grand, S. P. (2002), Mantle shear-wave tomography and the fate of subducted slabs, Philosophical Transactions of the Royal Society of London Series a-Mathematical Physical and Engineering Sciences, 360, 2475-2491.

Megnin, C., and B. Romanowicz (2000), The three-dimensional shear velocity structure of the mantle from the inversion of body, surface and higher-mode waveforms, Geophys. J. Int., 143, 709-728.

Ni, S., and D. Helmberger (2003), Ridge-like lower mantle structure beneath South Africa, J. Geophys. Res., 108(B2), 2094-2110.

Panning, M. P., and B. A. Romanowicz (2005), A three-dimensional radially anisotropic model of shear velocity in the mantle, Geophys. J. Int., in review.

Ritsema, J., et al. (1999), Complex shear wave velocity structure imaged beneath Africa and Iceland, Science, 286, 1925-1928.

Wen, L. X. (2001), Seismic evidence for a rapidly varying compositional anomaly at the base of the Earth's mantle beneath the Indian Ocean, Earth Planet. Sci. Lett., 194, 83-95.

Wysession, M. E. (1996), Large-scale structure at the core-mantle boundary from diffracted waves, Nature, 382, 244-248.

a) *SKS* *SKKS*   MSVF
105.8°
EV#16

b) *S*   HOPE
89.0°
EV#71

c) *S*   LCOL
95.9°
EV#38

d) *sSKS + Sd*   NOUC
112.0°
EV#6

e) *SPdKS* *SKKS*   TRIB
113.4°
Sd   EV#7

f) *SKKS*   DRV
97.1°
EV#46

— *SV*
···· *SH*

0   40   80   120

Relative time (s)
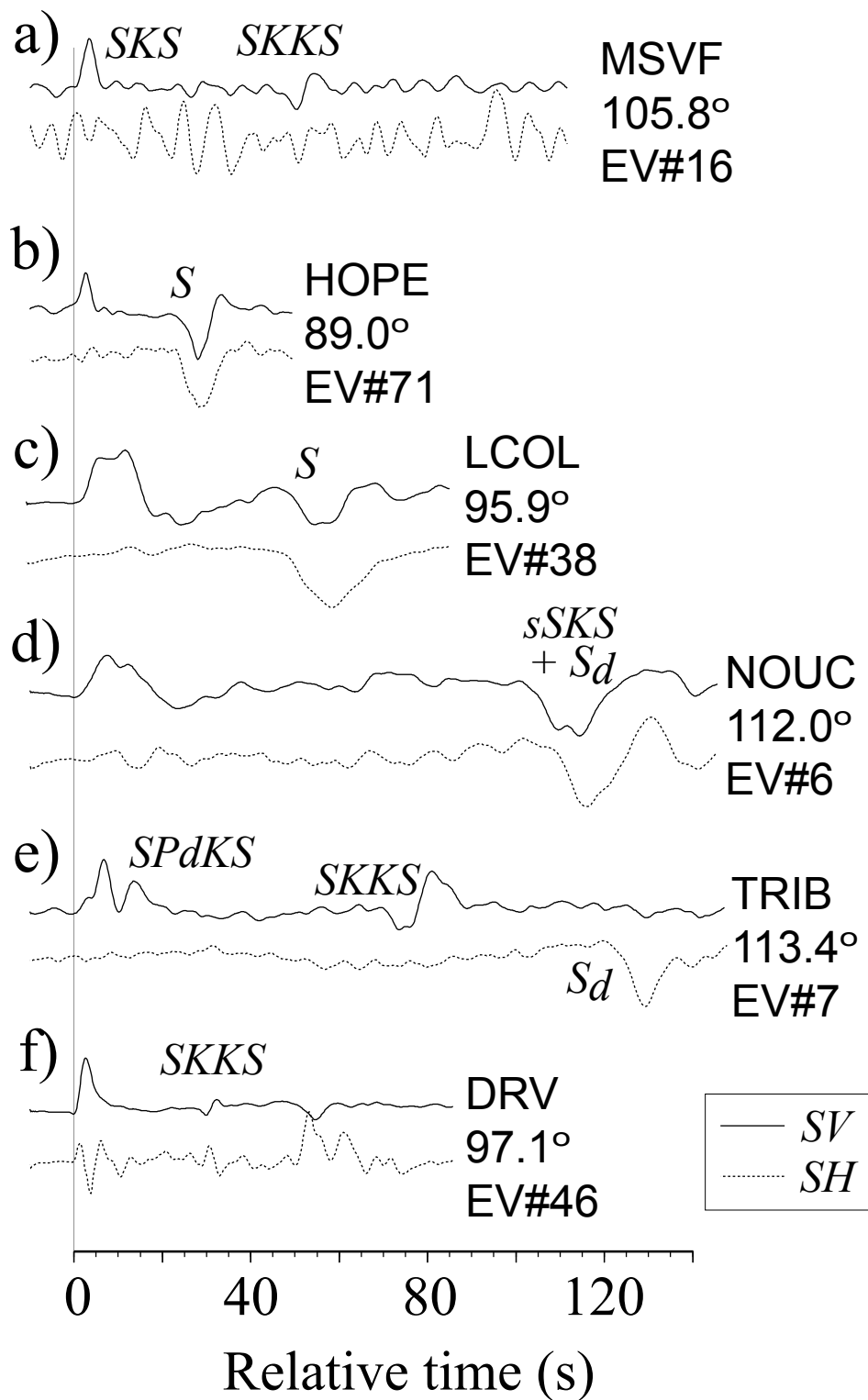
Figure A1
Ford et al. [2005]
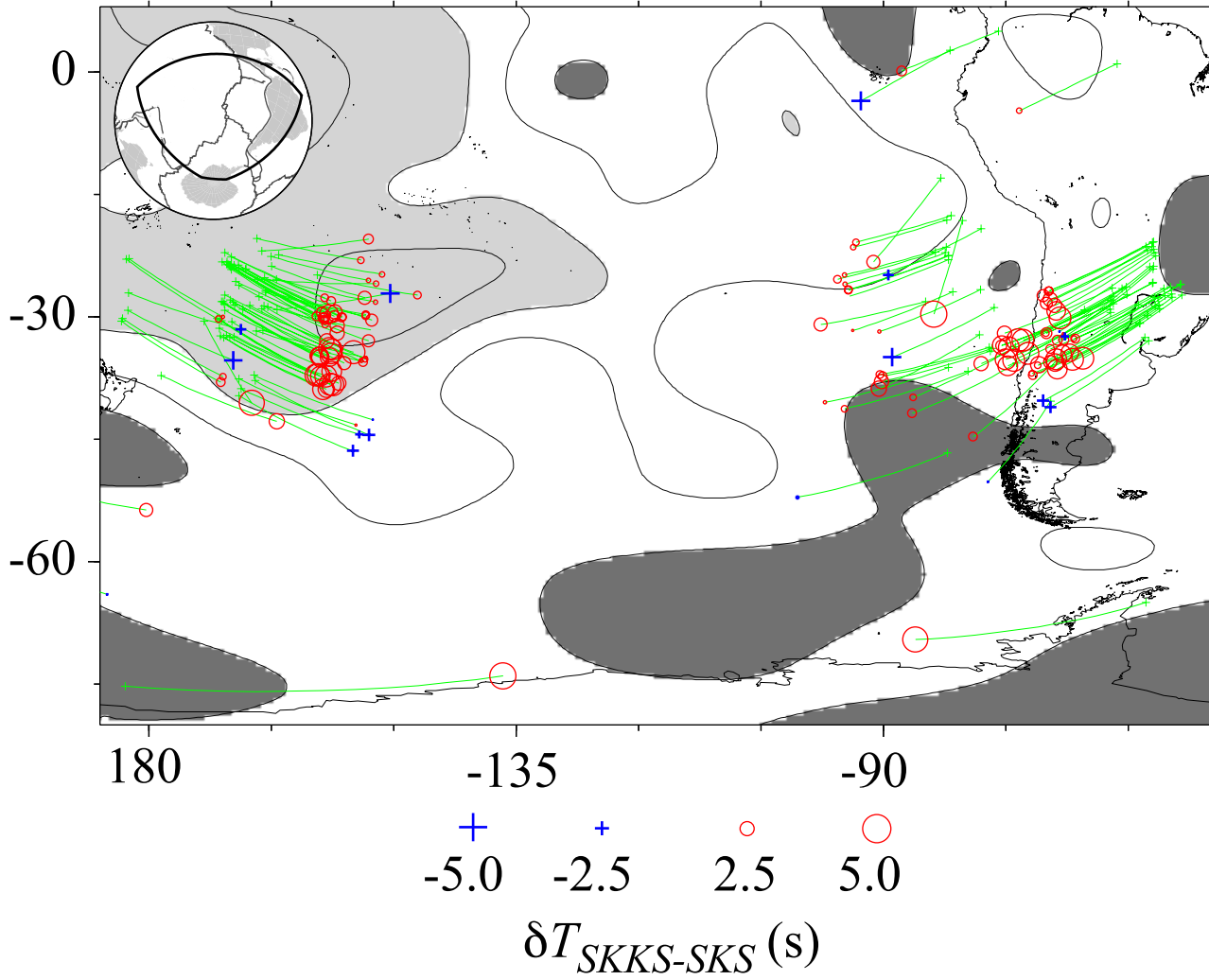
Figure A2
Ford et al. [2005]
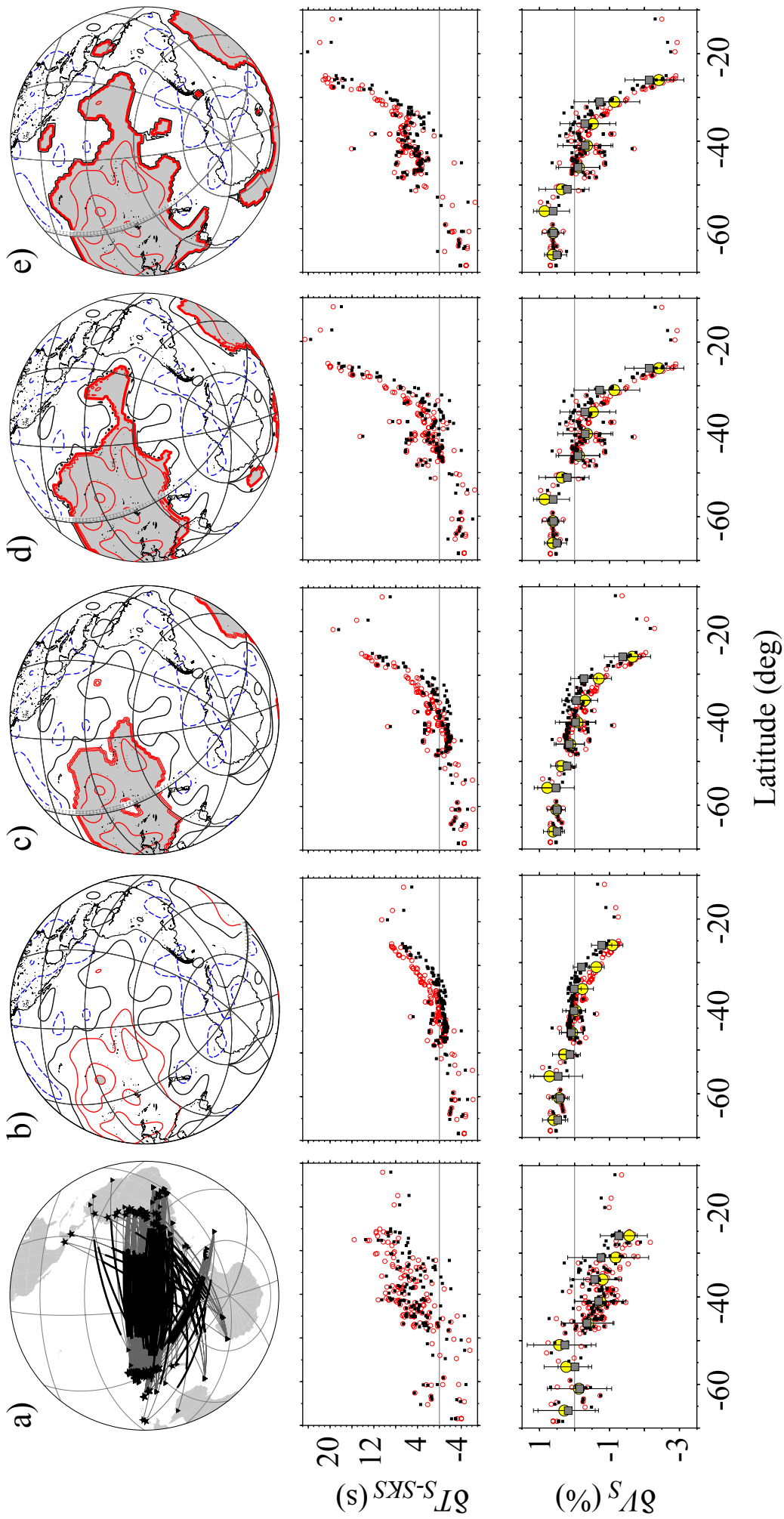
Figure A3
Ford et al. [2005]

Figure A4
Ford et al. [2005]